HHS Public Access

Author manuscript

Magn Reson Med. Author manuscript; available in PMC 2018 February 01.

Published in final edited form as:

Magn Reson Med. 2017 February ; 77(2): 730–739. doi:10.1002/mrm.26165.

On-resonance Variable Delay Multi Pulse Scheme for Imaging of Fast-exchanging Protons and semi-solid Macromolecules

Jiadi Xu[1,2,*,#], **Kannie W.Y. Chan**[1,2,#], **Xiang Xu**[1], **Nibhay Yadav**[1,2], **Guanshu Liu**[1,2], and **Peter C. M. van Zijl**[1,2]

[1]Russell H. Morgan Department of Radiology and Radiological Science, Johns Hopkins University School of Medicine, Baltimore, MD, USA

[2]F.M. Kirby Research Center for Functional Brain Imaging, Kennedy Krieger Research Institute, Baltimore, MD, USA

Abstract

Purpose—To develop an on-resonance variable delay multi-pulse (VDMP) scheme to image magnetization transfer contrast (MTC) as well as the chemical exchange saturation transfer (CEST) contrast of total fast-exchanging protons (TFP) with exchange rate above about 1 kHz.

Methods—A train of high power binomial pulses was applied at the water resonance. The inter-pulse delay, called mixing time, was varied to observe its effect on the water signal reduction, allowing separation and quantification of MTC and CEST contributions due to their different proton transfer rates. The fast-exchanging protons in CEST and MTC are labeled together with the short T_2 components in MTC and separated out using a variable mixing time.

Results—Phantom studies of selected metabolite solutions (glucose, glutamate, creatine, myo-inositol), bovine serum albumin (BSA) and hair conditioner show the capability of on-resonance VDMP to separate out exchangeable protons with exchange rates above 1 kHz. Quantitative MTC and TFP maps were acquired on healthy mouse brains using this method showing strong gray/white matter contrast for the slowly transferring MTC protons while the TFP map was more uniform across the brain but somewhat higher in gray matter.

Conclusions—The new method provides a simple way of imaging fast-exchanging protons, as well as MTC components with a slow transfer rate.

Keywords

Chemical Exchange Saturation Transfer (CEST); variable delay multi-pulse (VDMP); on-resonance VDMP; Quantitative Magnetization Transfer (qMT); Magnetization Transfer Contrast (MTC); Total Fast-exchanging Proton (TFP)

[*]**Corresponding Author:** Jiadi Xu, Ph.D., Kennedy Krieger Institute, Johns Hopkins University School of Medicine, 707 N. Broadway, Baltimore, MD, 21205, xuj@kennedykrieger.org, Tel: 443-923-9572, Fax: 443-923-9505.

[#]Authors contributed equally

INTRODUCTION

Chemical exchange saturation transfer (CEST) is an MRI technique that is capable of enhancing the MRI sensitivity of low concentration metabolites *in vivo* by making use of their exchangeable protons (1–3). The technique utilizes radiofrequency (RF) irradiation to saturate solute protons, most often in a frequency-selective off-resonance manner. This saturation is subsequently transferred to water through chemical exchange of these protons, resulting in a reduction in the water signal intensity. The CEST signal originates from the mobile proteins and metabolites in biological tissues, while conventional magnetization transfer effects originate from solid-like macromolecules, which are usually not directly observable by MRI due to their extremely short T_2 introduced by the strong dipolar couplings among the protons. Exchange and dipolar transfer are two types of magnetization transfer (MT) and in order to distinguish them, we specify the latter mechanism as magnetization transfer contrast (MTC), following a convention we set in earlier work (2). Both CEST and MTC contrasts, sometimes convolved, have been shown to be sensitive to pathological changes in tissues, such as neurological disorders (4–7), stroke (8–10), cancer (11–16), cardiac fibrosis (17) intervertebral disc diseases (16,18,19) and renal failure (20).

CEST experiments are usually performed in a way closely resembling those for MTC and saturation using RF pulses causes direct water saturation (DS), MTC, and CEST contrast to occur simultaneously. To reduce MTC contributions and the width of the DS lineshape in CEST studies, it is common to apply low power saturation pulses (21–23). This strategy works well for slow-exchanging protons, such as amide proton transfer (APT) CEST and relayed nuclear overhauser effect (rNOE) CEST (2,24–26). However, adequate saturation of fast-exchanging protons during their short life time on the low-concentration compound requires a high B_1 field, which increases MTC effects and the water DS line-width, and hence obscures the CEST signal. This seriously hampers the application of the CEST technique for imaging fast-exchanging protons at clinical field strengths, especially hydroxyl and amine groups for which the offsets are within a few hundred Hertz from the water resonance at 3T.

We propose an on-resonance version of the variable delay multi-pulse (VDMP) CEST approach (24), in which a train of high-B_1 binomial pulses is applied with the offset on the water resonance and with a range of inter-pulse delays, i. e. mixing times. The mixing times are varied in a manner similar to those used in the off-resonance VDMP sequence (24). The binomial pulses act as labeling pulses for the fast-exchanging protons with minimal perturbation of the water signal. Since the inherent T_2 of macromolecules in tissue is on the order of 20 μs, they are also labeled by the same binomial pulses, but by efficient dephasing of the excited transverse magnetization, which is the basis of pulsed MTC studies (23,27–33). On-resonance saturation with binomial pulses has previously been proposed for MTC studies (27–30,34,35). However, these methods either apply a single labeling pulse (29,34,35), which has much less MTC effect, or utilize multiple pulses or binomial pulses with a fixed inter-pulse delay (30,33). Previous efforts have focused on extracting information about the MTC pool with relatively slow intermolecular saturation transfer (exchange) rates. The fast-exchanging protons are usually assumed to be part of the MTC pool, i.e. a simple two-pool model with population averaged rate is used, which not only

ignores the important information about the metabolites in tissue, but also induces errors when estimating the multiple pool size and exchange parameters for quantification of MTC pool. The proposed method here can separate the slow MTC pool and fast-exchanging tissue pool unambiguously by fixing the pulse number and varying the mixing time, which is used as an exchange rate or dipolar transfer rate filter to separate the two pools based to their unique characteristic buildup patterns as a function of mixing time (24).

An on-resonance pulse train for CEST studies has been proposed previously for detecting paraCEST agents (36–38). Using a train of weak on-resonance pulses (< 8 μT) with compensatory phases to achieve a zero flip angle for water magnetization, the slow-exchanging water protons are restored to the initial state, while a small water signal loss occurs in the presence of the paraCEST agent (often > 10^4 Hz) due to its rapidly exchanging water molecules leaving the contrast agent during the pulses. More recently, use of an on-resonance binomial pulse was introduced in the on-resonance frequency labeled exchange (FLEX) technique (39) and the so-called transfer rate edited (TRE) CEST experiment (40). In the FLEX version, a long train of on-resonance pulse-pairs (90° / −90°) is applied, and the exchanging protons are labeled by varying the evolution time between these pulses, which is followed by a constant exchange time (mixing time). Each pulse sequence section contains an individual pulse-pair followed by a mixing time, which is called a label transfer module (LTM). A short RF excitation pulse duration usually is applied (0.02 ms), allowed rapidly exchanging protons to be labeled efficiently. The on-resonance VDMP scheme we propose here, which can be seen as the FLEX sequence with zero evolution time between the pulses, consists of a series of LTMs with binomial pulses of longer duration (2 ms) used to label the fast-exchanging protons. However, the labeling strategy proposed in current method is significantly different from the FLEX scheme. Since the evolution time is negligible, the CEST labeling is achieved only using the pulse profile of the binomial pulses, and is excitation based which is why the pulses are lengthened relative to the FLEX. For the semi-solid MTC, labeling occurs both through dephasing of the transverse component and saturation. Since the saturation is not frequency selective, all fast-exchanging protons contribute to the signal. We first validate this technique on several common metabolites, a protein (bovine serum albumin, BSA) and MTC phantoms (cross-linked BSA and hair conditioner) to show the effectiveness in separating fast-exchanging protons and slow MTC effects. We then perform in vivo mapping of the signal contributions of both the total fast-exchanging protons (TFP) and the slowly-transferring MTC pool in mouse brain.

METHODS

Pulse Sequence

The on-resonance VDMP pulse sequence used for this study is similar to the off-resonance VDMP sequence (24), i. e., a train of high power pulses with proper mixing time followed by an image acquisition module (Fig. 1A). In the current study, a simple binomial pulse composed of two high power pulses with alternating phase ($p\bar{p}$) was used instead of the single pulse in the conventional VDMP approach, thus also resembling the on-resonance FLEX with zero mixing time (39). The phases of the binomial pulse pairs were cycled between each pulse unit (label transfer module or LTM) to suppress any residual

magnetization in the transverse plane and related image artifacts (41). Although other frequency-selective pulses can be used for on-resonance saturation, binomial pulses are very suitable to minimize direct water excitation and the effect of B_1 inhomogeneity. Similar to off-resonance VDMP, the number of pulses was fixed while the mixing time was varied. The observed MTC/CEST signal as a function of mixing time, i. e., the VDMP build-up curve, can be calculated using the coupled Bloch equations for a two-pool model (27):

$$\mathrm{d}\,\vec{M} = \Lambda\,\vec{M}$$

$$\vec{M} = \begin{bmatrix} M_w(t) \\ M_s(t) \end{bmatrix}$$

$$\Lambda = \begin{bmatrix} R_{1w}+k_w & -k_s \\ -k_w & R_{1s}+k_s \end{bmatrix} \quad (1)$$

where $M_w(t)$ and $M_s(t)$ refer to the water and solute proton magnetization, respectively. k_s is the small pool to water exchange rate for the MTC or CEST pool, and x_s is the fractional concentration of the transferrable protons of these two pools relative to that of the water protons. After each binomial pulse, the saturation becomes $\alpha_s M_s(0)$ in which α_s denotes the saturation efficiency of the transferring protons (CEST and MTC in this case), which depends on the power of the RF pulse, the pulse width and the exchange (transfer) rate k. The water magnetization $M_w(t)$ is also attenuated by α_w due to the water direct saturation, and the total water saturation is proportional to the sum of both effects integrated over the total number of LTMs used. During the mixing time the magnetizations $M_w(t)$ and $M_s(t)$ evolve according to Eq. 1. The above equation can be easily extended to a three-pool model, where two pools represent slow and fast-exchanging protons, $M_{s,slow}(t)$ and $M_{s,fast}(t)$, respectively, with concentrations $x_{s,slow}(x_{s,fast})$ and exchange rates $k_{s,slow}(k_{s,fast})$.

$$\mathrm{d}\,\vec{M} = \Lambda\,\vec{M}$$

$$\vec{M} = \begin{bmatrix} M_w(t) \\ M_{s,\mathrm{slow}}(t) \\ M_{s,\mathrm{fast}}(t) \end{bmatrix}$$

$$\Lambda = \begin{bmatrix} R_{1w}+k_{w,\mathrm{slow}}+k_{w,\mathrm{fast}} & -k_{s,\mathrm{slow}} & -k_{s,\mathrm{fast}} \\ -k_{w,\mathrm{slow}} & R_{1s,\mathrm{slow}}+k_{s,\mathrm{slow}} & 0 \\ -k_{w,\mathrm{fast}} & 0 & R_{1s,\mathrm{fast}}+k_{s,\mathrm{fasl}} \end{bmatrix} \quad (2)$$

Usually, the exchange rates $k_{s,slow}$ and $k_{s,fast}$ are much larger than the R_{1s} of transferring protons. Therefore, knowledge of the relaxation times $R_{1s,slow}$ ($R_{1s,fast}$) is not necessary for the calculation of the VDMP buildup curves by assuming $R_{1s} + k_s \approx k_s$. The slow-exchanging (slow transfer) pool in principle has contributions from any slow exchanging protons, including those from metabolites, the conventional MTC pool and the relayed NOE (rNOE) CEST pool (42). However, because the labeling of the MTC protons is instantaneous (T_2 dephasing) and their pool size very large (~7–13% of the water signal in gray and white matter, respectively) (27,43), their contribution dominates over other slow-exchanging protons for which the concentration is in the millimolar range and saturation efficiency low. We describe the slowly transferring pool "s = *slowMTC*" with a corresponding fraction $x_{slowMTC}$ and the exchange rate is $k_{slowMTC}$. The total pool of fast exchanging protons (metabolites plus some MTC from fast-exchanging OH or amine protons in the semi-solid) is named the total fast-exchanging proton (TFP) pool "s = TFP" with concentration x_{TFP}. Neglecting T_1 and back exchange effects, the effect size basically is proportional to $\alpha_s x_s$, but saturation efficiencies and concentrations cannot be separated out in the current method where only a single saturation power is applied, while exchange rates in the appropriate range can be separated out by varying the mixing time. Therefore, the saturation efficiency was assumed to be 1 for MTC when using high power excitation pulses and exploiting the extremely short T_2 of the MTC pool. However, as mentioned above, the effective saturation efficiency of the fast-exchanging protons is a function of the exchange rate. Therefore, an $\bar{\alpha}_{TFP} x_{TFP}$ map will be calculated instead to reflect the combined effects of proton concentration, and effective saturation efficiency ($\bar{\alpha}_s$).

Simulations

The VDMP buildup curves were simulated for protons with different exchange rates to demonstrate the feasibility of distinguishing the exchanging proton pools by their unique VDMP buildup patterns. The pulse profile of the $p\bar{p}$ binomial pulse was calculated for three typical pools: water protons, slowMTC protons and fast-exchanging protons. The pulse excitation profile is critical for choosing a proper saturation power for the binominal pulses. The excitation around zero frequency for the water pool should be minimized and uniform to avoid image intensity variation due to B_0 inhomogeneity. Two saturation power levels, 93.6 μT and 23.4 μT, with fixed pulse duration of 2 ms were simulated to represent high and relatively low power situations. For fast-exchanging protons, the CEST signal will be higher with longer saturation pulses considering the excitation bands are close to water. On the other hand, long pulses also cause significant water direct saturation around zero frequency. A pulse width of 2 ms was found to a good balance between these two factors.

In Vitro Phantom Experiments

Glucose (Glc, 50 mM and 200 mM), glutamate (Glu, 50 mM), creatine (Cr, 50 mM), myo-inositol (mI, 50 mM), bovine serum albumin (BSA, 10%w/v), cross-linked BSA (10%w/v) and hair conditioner (Suave) were selected to represent metabolites found in tissue, as well as a mobile protein and MTC pools. The hair conditioner contains a lamellar structure similar to membranes in neural tissues (44,45). Except for the hair conditioner, phantoms were prepared in phosphate buffered saline (PBS), titrated to pH 7.3, and transferred to 5 mm NMR tubes. The cross-linked BSA was prepared by incubating the tubes in 80°C water

for 10 min followed by slow cooling. All MRI experiments were performed on a horizontal bore 11.7 T Bruker Biospec system (Bruker, Ettlingen, Germany) equipped with actively shielded gradients of maximum strength 74 Gauss/cm. A 23 mm volume transceiver coil was used, and images were acquired using a RARE sequence with TR/TE=10 s/4 ms, RARE factor=32, slice thickness=2 mm, a matrix size of 64×64 within a FOV of 1.8×1.8 cm^2. For the saturation part, 4 and 32 binomial pulses with mixing times ranging from 0 ms to 130 ms were applied. The pulse width was 2 ms with B_1 of 93.6 μT. Here, a high saturation power was applied to achieve sufficient saturation of fast exchanging protons on solutes. The T_1 relaxation times of the mouse brain and phantoms were measured using variable TR (TR=0.5, 1, 1.5, 2, 3.5, 5, 8 s) with the aforementioned imaging parameters. The T_2 relaxation times were measured using a nonselective Carr-Purcell-Meiboom-Gill preparation module followed by a RARE readout (46).

In Vivo Animal Studies

The institutional animal care and use committee approved this study. Three adult female BALB/c mice (10–18 weeks) were used for testing the on-resonance VDMP method. All animals were anesthetized using 2 to 2.5% vaporized inhaled isoflurane, followed by 1% to 1.5% isoflurane during the MRI scan. Mice were positioned with a bite bar and ear pins and placed on a water-heated animal bed equipped with temperature and respiratory control. Images were acquired using a 72 mm quadrature volume resonator as transmitter, and a 4-element (2×2) phased array coil. The B_0 field over the mouse brain was adjusted using field mapping and global shimming up to second order. Images were acquired using a RARE sequence with TR/TE= 8 s/ 4 ms, RARE factor= 8, slice thickness =1 mm, a matrix size of 64 × 64 within a FOV of 1.2×1.2 cm^2. Four and 32 binomial pulses (B_1=93.6 μT; 2 ms pulse width) with 10 mixing times ranging from 0 to 150 ms were used for slowMTC and TFP quantification, respectively.

Data Analysis

Data were analyzed with custom-written MATLAB scripts. The Matlab code used for fitting the VDMP buildup curves can be found in the supplemental materials. The VDMP buildup curves acquired using four binomial pulses for both phantom and mouse brain were fitted for $x_{slowMTC}$ and $k_{slowMTC}$. Four pulses suffice due to the high MTC fraction and efficient saturation through T2 dephasing. Although, the curves can also be fitted using a three-pool model similar to the situation with 32 pulses, the contribution from the TFP pool is negligible due to the low number of pulses. Therefore, a two-pool model (slowMTC pool and water pool) was used for fitting VDMP buildup curves with four binomial pulses. The water DS and water signal attenuation due to saturation and transfer of fast-exchanging protons was assumed to be constant for different mixing times, which is valid assumption when the number of labeling pulses is small (total water saturation buildup time is less than 600 ms when four binomial pulses are applied). When fitting the VDMP buildup curves acquired with 32 pulses, three variable parameters ($x_{slowMTC}$, $k_{slowMTC}$, $\bar{a}_{TFP}x_{TFP}$) were used in the fitting with a three-pool model. The measured T_1 values obtained using the variable-TR RARE sequence were used in the fitting. Both water direct saturation and saturation transfer from fast-exchanging protons attenuate the water signal during the labeling pulses while T_1 recovery occurs between the pulses. Therefore, DS and T_1 effects

are not distinguishable by varying the mixing time in the on-resonance VDMP technique. The observed water saturation efficiency will be a combined effect between water DS efficiency (small due to the use of binomial pulses) and saturation transfer efficiency of the TFP pool. Since exchange occurs rapidly during the pulses, no new saturation is transferred during the mixing time and the signal decay of the fast-exchanging protons during the mixing time is independent of the exchange rate and depends only on water T_1 (47). An average exchange rate of 5 kHz was assumed for the fast-exchanging protons considering the VDMP buildup curve is approximately independent of exchange rate when higher than 1 kHz (Fig. 1). The fitting on phantoms takes about 96 s with the two-pool model, and takes about 868 s for the three-pool model on a Macbook pro (2.7GHz dual-core Intel Core i5) computer. The parameters were extracted using nonlinear least-squares curve fitting method with a termination tolerance of 10^{-3} for the function value.

RESULTS

Simulations

In Figs. 1B&C simulations of the VDMP buildup curves as a function of mixing time are shown for protons with different exchange rates using a VDMP sequence with 32 and 4 pulses of 2 ms length and a B_1 of 93.6 μT. It can be seen that the curve shape is sensitive to the exchange rate of slow-exchanging protons, but almost identical for exchange rates higher than 1 kHz, since the transfer of saturation happens only during the pulses. In Figs 2A and 2B, the saturation profiles for water at pulse powers 93.6 μT and 23.4 μT, respectively, are shown. A more uniform low saturation around water is achieved with high power pulses. The pulse saturation profile is critical when using a large number of binomial pulses, since the image artifacts due to B_0 variation can accumulate and cause some black band artifacts. From testing different B_1 values on the mouse brain, we found that images were artifact free when B_1 was higher than 46.8 μT, in line with these simulations. The simulations in Fig. 2C show that the MTC pool with short T_2 (0.02 ms) can be fully saturated by high power binomial pulses (>93.6μT) However, the saturation profile of the binomial pulse on the exchanging protons is a complicated function of the exchange rate and saturation power (see Figs. 2E and 2F). When the exchange rate is zero, the saturation profile is identical to the periodical pulse profile measured by changing the water resonance frequency, with its maximum located at the offset of the exchangeable protons of interest (2 ppm here). At higher exchange rates, when the exchange regime changes from slow to intermediate to fast, the exchangeable proton and water proton resonances begin to merge in a manner proportional to the pool populations, effectively shifting the saturation profile towards water. In Fig. 2G, the saturation effect on water is simulated as a function of exchange rate for protons with a chemical shift offset of 2 ppm. Contrary to the MTC pool, a high saturation efficiency is achieved for relatively low saturation power and high exchange rate (> 2 kHz), which will allow us to separate out the slowly exchanging MTC pool from the total fast exchanging proton pool.

Figure 3A illustrates a simulation of the observed CEST/MT signal when taking DS, slowMTC and TFP contributions into account. In the simulations, parameters typically obtained for cross-linked BSA were applied, i. e. $x_{slowMTC} = 10\%$, $k_{slowMTC} = 50\ HZ$, $T_1 = 2$

s and T_2 = 50 ms. The DS was assumed to be a single exponential decay curve, while the TFP and slowMT was calculated using the two-pool model (Eq.1) and the above parameters. The observed signal was calculated using the three-pool model (Eq.2). At zero mixing time, the observed CEST/MT signal originates mainly from the DS and TFP pools. The contribution from slowMTC pool increases with longer mixing times, while that of the DS and FTP signals decreases. The time for the MT signal of slowMTC pool to reach maximum is determined by the exchange rates of the slowMTC pool.

Phantom Experiments

Figs. 3B and 3C show the on-resonance VDMP curves measured for the phantoms. Due to a significant amount of fast-exchanging protons in cross-linked BSA, the CEST/MTC signal at zero mixing time is already around 7.8 %, while it is only 1.2 % for hair conditioner. The signal of cross-linked BSA and hair conditioner builds up and then decays slowly with respect to the mixing time for both four (Fig. 3B) and 32 (Fig. 3C) saturation pulses. The parameters extracted by fitting the VDMP curves using two-pool and three-pool models are listed in Table 1. The $x_{slowMTC}$ and $k_{slowMTC}$ obtained using both four and 32 saturation pulses are comparable. The hair conditioner exchange rate (22 Hz) was around half of that of cross-linked BSA (50 Hz), while the $x_{slowMTC}$ were similar for both MTC phantoms. The exchange rate of cross-linked BSA is in agreement with the values measured previously using the selective inversion recovery method (45 Hz) (48) and CW-CEST (43 Hz) (49). Figure 3E shows the $x_{slowMTC}$ map determined using four binomial pulses. The metabolites are not visible in the $x_{slowMTC}$ map with the limited number of pulses. BSA solution only shows weak $x_{slowMTC}$ (mainly from rNOE-CEST) due to the low labeling efficiency of the mobile protein by the binomial pulses.

On the other hand, signal from fast-exchanging protons, such as those in Glc and Glu, only decays when the mixing time increases (Fig. 3C). Therefore, the $x_{slowMTC}$ values are close to zero for the metabolites. The $\bar{\alpha}_{TFP}x_{TFP}$ map displayed in Fig. 3F was calculated using the three-pool model with 32 saturation pulses. Among the metabolites studied, Glu gave the highest $\bar{\alpha}_{TFP}x_{TFP}$ value, which was due to the higher exchange rate (around 5.5 kHz) of the amine group (50). The exchange rates of the hydroxyl groups in mI and Glc are only around 1–2 kHz (13,51) therefore resulting in lower saturation efficiency (Fig. 2G), i. e. weaker $\bar{\alpha}_{TFP}x_{TFP}$ signal. Cr also show weak contrast in the $\bar{\alpha}_{TFP}x_{TFP}$ map with the guanidine groups exchanging only at a few hundred Hz (52). The concentrations and exchange rates of the slow-exchanging protons can only be reliably obtained when the initial buildup process in the onVDMP curves resembles the simulations in Fig. 1B. The exchange rate of amine groups in Cr is already beyond the detection limit of current method, i. e. no buildup process was observed for the Cr phantom. Although, the majority signal in hair conditioner comes from slow-exchanging protons from the aliphatic protons of the lipids, there are still OH and NH protons in the lipid head groups, which explains the relatively high $\bar{\alpha}_{TFP}x_{TFP}$ value in the hair conditioner. The $\bar{\alpha}_{TFP}x_{TFP}$ is proportional to the concentration of the metabolites as seen from the values of 50 mM (0.19) and 200 mM Glc (0.74) solutions. It is also interesting to note the strong effect of the OH exchange on the T_2 in a manner proportional to concentration (53,54).

In Vivo Imaging of Mouse Brain

The on-resonance VDMP sequence was tested on the brains of healthy mice to estimate the $x_{slowMTC}$, $k_{slowMTC}$ and $\bar{a}_{TFP}x_{TFP}$ values. The parametric maps of $x_{slowMTC}$ and $k_{slowMTC}$ obtained from saturation with four binomial pulses and fitted with a two-pool model are shown in Figs. 4A,B. The $x_{slowMTC}$, $k_{slowMTC}$ and $\bar{a}_{TFP}x_{TFP}$ maps generated by fitting a three-pool model to on-resonance VDMP data acquired using 32 binomial pulses are shown in Figs. 5A–C, respectively, and the values are reported in Table 2. The mixing time dependencies of signals from the cortex (cx) and thalamus (th) (Fig. 4D) resemble the one obtained from cross-linked BSA. The $k_{slowMTC}$ values were of comparable magnitude when applying four and 32 saturation pulses, but the fractions $x_{slowMTC}$ were quite different. The exchange rate $k_{slowMTC}$ of the muscle (around 50 Hz) is much higher than that of brain. Therefore, the edge of the mouse brain sometime shows high exchange rates due to a partial volume effect. The $\bar{a}_{TFP}x_{TFP}$ map is presented in Fig. 5C, showing uniform signal across the brain with an average value of 3.0± 0.15 %. A small signal drop-off is visible in areas with low SNR further away from the receive coil.

DISCUSSION

We designed an on-resonance VDMP scheme to separate and quantify the slowMTC and TFP fractions in the brain. The binomial saturation pulses in this approach, which are similar to the ones used in FLEX except for their length, could achieve much higher labeling efficiency for fast-exchanging protons and the MTC than conventional CW or pulsed CEST techniques. By applying an appropriate number of pulses and varying the mixing times, the exchangeable proton pools with different exchange rates, such as TFP and slowMTC pools could be well distinguished and quantified.

In phantoms, metabolites with fast exchanging protons such as Glu and Glc could be highlighted with a series of 32 binomial pulses (Figs. 3E&3F), while the macromolecules such as cross-linked BSA and lipids (hair conditioner) were already visualized with four pulses. Proteins containing both fast and slow-exchanging protons showed high signal under both situations. Both BSA and cross-linked BSA show high $\bar{a}_{TFP}x_{TFP}$ signal due to the abundant amine groups on the protein (Table 1). The high signal of cross-linked BSA compared to the same concentration of BSA solution (see Fig. 3 E&F) is most likely due to the efficient saturation with T_2 dephasing in the semi-solid material..

The brain contains a diversity of exchanging protons. Based on the current and previous studies (42,45,55), three major components with approximately distinct exchange rate ranges can be found in brain: (I) myelin lipids from galacto-cerebrosides and cholesterols with slow dipolar exchange rates (< 20 Hz) (45,55); These also contain fast-exchanging protons such as OH groups. (II) small metabolites, some of which contain a large number of fast-exchanging protons; (III) Proteins with a variety of molecular sizes contribute to both slow and fast-exchanging protons. There also are some metabolites with slower exchange rates, such as phosphate creatine (pCr) and creatine (Cr). The concentration of those compounds is low compared to that of the total number of protons in proteins. Therefore, they will not be discussed here. The aliphatic protons in proteins with large molecular size can also exchange with water by a relayed dipolar transfer process through all types of

exchanging protons (mainly amide protons) (2,42), which exchange at a rate similar to dipolar exchange in myelin lipids (45). These relayed slow exchanging protons have an exchange rate on the order of 40–50 Hz as measured in cross-linked BSA (see Table 1)(24). However, the exchange rate will be significantly lower (< 20 Hz) for mobile proteins due to the weak intramolecular dipolar coupling as seen from the BSA solution (24). The fast-exchanging protons, such as the hydroxyl and amine groups on proteins have exchange rates of 1 kHz and higher. As transfer of saturation of fast exchanging protons only happens during the labeling pulses, the fast-exchange component can be significantly suppressed when only few binomial pulses are applied in the on-resonance VDMP (Fig. 3E).

These basic mechanisms were also apparent in the brain studies. E.g. when four binomial pulses were applied (Fig. 4), we mainly detected the slow exchanging components from myelin lipids (I) and large proteins (III), which displayed a lower average exchange rate, $\bar{k}_{slowMTC}$, e. g. the areas of the brain where myelin is abundant such as thalamus and corpus callosum (Fig. 4B). Interestingly, this exchange rate is much lower than the reported values in qMT studies by the pulsed MT method (50–60 Hz) (27,32,43,56). In most of qMT studies, a simple two-pool model is used for fitting. Therefore, the measured exchanged rate is an averaged value between slowMTC and TFP pools. The slow exchange rate of the slowMTC pool indicates that the major contribution to slowMTC is from the myelin lipids (component I), which is consistent with the observation that the WM fraction is highlighted in the image. Similar $k_{slowMTC}$ values were found when applying four and 32 saturation pulses.

The range of $x_{slowMTC}$ values found (Table 2) is quite consistent with previous quantitative magnetization transfer (qMT) studies, where $x_{slowMTC}$ was around 6–8% for grey matter and 11–15% for white matter (32), Interestingly, however, these fractions $x_{slowMTC}$ were quite different when using a different number of pulses. We tentatively attribute this to the fact that when a large number of pulses is applied, the longer T_2 components, such as mobile proteins, will also contribute to the signal. Therefore, the $x_{slowMTC}$ increases slightly with higher pulse number. The $\bar{\alpha}_{TFP}x_{TFP}$ map (Fig. 5C), which is an indication of the mobile protein concentration (component III) and the metabolites (component II), is quite uniform across brain in line with recent studies using off-resonance VDMP (57) and MRS (58) techniques.

The binomial pulse is designed to label all exchanging protons in a way depending on the excitation profile, except the water resonance (see Fig. 2). In our study on a preclinical scanner, simple $p\bar{p}$ type binomial pulses were applied due to their ease of setup and their inherent property that the B_1 inhomogeneity can be compensated. The pulse power and length need to be optimized to achieve the desired labeling frequencies for a particular CEST application and field strength, and to minimize direct water saturation. In the current study, we found negligible image artifacts with the combined use of phase cycling and crusher gradients. However, when applying the method on clinical scanners, while benefitting from improved B_1 and B_0 homogeneity, the frequency difference with water protons is smaller and the available maximum B_1 is much less (~20 μT). Fortunately, the simulations in Fig. 2 demonstrate that, for lower saturation powers, the excitation maxima of the binomial pulse profile are shifted towards the water resonance,, which is thus beneficial

for application at clinical scanners. However, at lower field, more sophisticated binomial pulses or selective pulses may need to be implemented to optimize the frequency band-stop around the water frequency.

CONCLUSION

The on-resonance VDMP technique proposed provides a simple and comprehensive way of separately mapping slow and fast-exchanging protons in tissues. Besides the quantification of the exchange rate together with macromolecule fraction, this technique can provide further information about the metabolites in tissues. Although the total fast-exchanging proton pool can be mapped, further study is still needed to correlate the map with the exact concentration of a set of metabolites.

Acknowledgments

This study was supported by NIH R01EB019934 (NIBIB), P50CA103175 (NCI), R01EB015032 (NIBIB), S10RR028955 (NCRR) and R21EB018934 (NIBIB).

REFERENCES

1. Ward KM, Aletras AH, Balaban RS. A New Class of Contrast Agents for MRI Based on Proton Chemical Exchange Dependent Saturation Transfer (CEST). J Magn Reson. 2000; 143(1):79–87. [PubMed: 10698648]
2. van Zijl PCM, Yadav NN. Chemical exchange saturation transfer (CEST): What is in a name and what isn't? Magn Reson Med. 2011; 65(4):927–948. [PubMed: 21337419]
3. Liu G, Song X, Chan KW, McMahon MT. Nuts and bolts of chemical exchange saturation transfer MRI. NMR Biomed. 2013; 26(7):810–828. [PubMed: 23303716]
4. Tozer D, Ramani A, Barker GJ, Davies GR, Miller DH, Tofts PS. Quantitative magnetization transfer mapping of bound protons in multiple sclerosis. Magn Reson Med. 2003; 50(1):83–91. [PubMed: 12815682]
5. Levesque IR, Pike GB. Characterizing healthy and diseased white matter using quantitative magnetization transfer and multicomponent T(2) relaxometry: A unified view via a four-pool model. Magn Reson Med. 2009; 62(6):1487–1496. [PubMed: 19859946]
6. Li C, Peng S, Wang R, Chen H, Su W, Zhao X, Zhou J, Chen M. Chemical exchange saturation transfer MR imaging of Parkinson's disease at 3 Tesla. European radiology. 2014; 24(10):2631–2639. [PubMed: 25038850]
7. Eckert T, Sailer M, Kaufmann J, Schrader C, Peschel T, Bodammer N, Heinze HJ, Schoenfeld MA. Differentiation of idiopathic Parkinson's disease, multiple system atrophy, progressive supranuclear palsy, and healthy controls using magnetization transfer imaging. Neuroimage. 2004; 21(1):229–235. [PubMed: 14741660]
8. Zhou J, Payen JF, Wilson DA, Traystman RJ, van Zijl PC. Using the amide proton signals of intracellular proteins and peptides to detect pH effects in MRI. Nat Med. 2003; 9(8):1085–1090. [PubMed: 12872167]
9. Sun PZ, Zhou J, Sun W, Huang J, van Zijl PCM. Detection of the ischemic penumbra using pH-weighted MRI. J Cereb Blood Flow Metab. 2006; 27(6):1129–1136. [PubMed: 17133226]
10. Jin T, Wang P, Zong X, Kim S-G. Magnetic resonance imaging of the Amine–Proton EXchange (APEX) dependent contrast. NeuroImage. 2012; 59(2):1218–1227. [PubMed: 21871570]
11. Zhou J, Lal B, Wilson DA, Laterra J, van Zijl PCM. Amide proton transfer (APT) contrast for imaging of brain tumors. Magn Reson Med. 2003; 50(6):1120–1126. [PubMed: 14648559]
12. Jia G, Abaza R, Williams JD, Zynger DL, Zhou J, Shah ZK, Patel M, Sammet S, Wei L, Bahnson RR, Knopp MV. Amide proton transfer MR imaging of prostate cancer: a preliminary study. J Magn Reson Imaging. 2011; 33(3):647–654. [PubMed: 21563248]

13. Chan KWY, McMahon MT, Kato Y, Liu GS, Bulte JWM, Bhujwalla ZM, Artemov D, van Zijl PCM. Natural D-glucose as a biodegradable MRI contrast agent for detecting cancer. Magn Reson Med. 2012; 68(6):1764–1773. [PubMed: 23074027]
14. Donahue MJ, Donahue PC, Rane S, Thompson CR, Strother MK, Scott AO, Smith SA. Assessment of lymphatic impairment and interstitial protein accumulation in patients with breast cancer treatment-related lymphedema using CEST MRI. Magn Reson Med. 2015 10.1002/mrm.25649.
15. Cai K, Singh A, Poptani H, Li W, Yang S, Lu Y, Hariharan H, Zhou XJ, Reddy R. CEST signal at 2ppm (CEST@2ppm) from Z-spectral fitting correlates with creatine distribution in brain tumor. NMR Biomed. 2015; 28(1):1–8. [PubMed: 25295758]
16. Desmond KL, Moosvi F, Stanisz GJ. Mapping of amide, amine, and aliphatic peaks in the CEST spectra of murine xenografts at 7 T. Magn Reson Med. 2014; 71(5):1841–1853. [PubMed: 23801344]
17. Vandsburger M, Vandoorne K, Oren R, Leftin A, Mpofu S, Delli Castelli D, Aime S, Neeman M. Cardio-chemical exchange saturation transfer magnetic resonance imaging reveals molecular signatures of endogenous fibrosis and exogenous contrast media. Circulation Cardiovascular imaging. 2014; 8(1):pii: e002180.
18. Liu Q, Tawackoli W, Pelled G, Fan Z, Jin N, Natsuaki Y, Bi X, Gart A, Bae H, Gazit D, Li D. Detection of low back pain using pH level-dependent imaging of the intervertebral disc using the ratio of R1rho dispersion and -OH chemical exchange saturation transfer (RROC). Magn Reson Med. 2015; 73(3):1196–1205. [PubMed: 24700573]
19. Ling W, Regatte RR, Navon G, Jerschow A. Assessment of glycosaminoglycan concentration in vivo by chemical exchange-dependent saturation transfer (gagCEST). Proc Natl Acad Sci U S A. 2008; 105(7):2266–2270. [PubMed: 18268341]
20. Longo DL, Busato A, Lanzardo S, Antico F, Aime S. Imaging the pH evolution of an acute kidney injury model by means of iopamidol, a MRI-CEST pH-responsive contrast agent. Magn Reson Med. 2013; 70(3):859–864. [PubMed: 23059893]
21. Jones CK, Polders D, Hua J, Zhu H, Hoogduin HJ, Zhou J, Luijten P, van Zijl PC. In vivo three-dimensional whole-brain pulsed steady-state chemical exchange saturation transfer at 7 T. Magn Reson Med. 2012; 67(6):1579–1589. [PubMed: 22083645]
22. Sun PZ, Benner T, Kumar A, Sorensen AG. Investigation of optimizing and translating pH-sensitive pulsed-chemical exchange saturation transfer (CEST) imaging to a 3T clinical scanner. Magn Reson Med. 2008; 60(4):834–841. [PubMed: 18816867]
23. Desmond KL, Stanisz GJ. Understanding quantitative pulsed CEST in the presence of MT. Magn Reson Med. 2012; 67(4):979–990. [PubMed: 21858864]
24. Xu J, Yadav NN, Bar-Shir A, Jones CK, Chan KW, Zhang J, Walczak P, McMahon MT, van Zijl PC. Variable delay multi-pulse train for fast chemical exchange saturation transfer and relayed-nuclear overhauser enhancement MRI. Magn Reson Med. 2014; 71(5):1798–1812. [PubMed: 23813483]
25. Jin T, Wang P, Zong X, Kim S-G. MR imaging of the amide-proton transfer effect and the pH-insensitive nuclear overhauser effect at 9.4 T. Magn Reson Med. 2013; 69(3):760–770. [PubMed: 22577042]
26. Jones CK, Huang A, Xu J, Edden RA, Schar M, Hua J, Oskolkov N, Zaca D, Zhou J, McMahon MT, Pillai JJ, van Zijl PC. Nuclear Overhauser enhancement (NOE) imaging in the human brain at 7T. NeuroImage. 2013; 77C:114–124.
27. Ropele S, Seifert T, Enzinger C, Fazekas F. Method for quantitative imaging of the macromolecular 1H fraction in tissues. Magn Reson Med. 2003; 49(5):864–871. [PubMed: 12704769]
28. Hu BS, Conolly SM, Wright GA, Nishimura DG, Macovski A. Pulsed saturation transfer contrast. Magn Reson Med. 1992; 26(2):231–240. [PubMed: 1325023]
29. Forster J, Schick F, Pfeffer M, Lutz O. Magnetization transfer by simple sequences of rectangular pulses. Magn Reson Med. 1995; 3(2):83–93.
30. Chai JW, Chen C, Chen JH, Lee SK, Yeung HN. Estimation of in vivo proton intrinsic and cross-relaxation rate in human brain. Magn Reson Med. 1996; 36(1):147–152. [PubMed: 8795033]

31. Graham SJ, Henkelman RM. Understanding Pulsed Magnetization Transfer. J Magn Reson Imaging. 1997; 7(5):903–912. [PubMed: 9307918]
32. Yarnykh VL. Pulsed Z-spectroscopic imaging of cross-relaxation parameters in tissues for human MRI: Theory and clinical applications. Magn Reson Med. 2002; 47(5):929–939. [PubMed: 11979572]
33. Pike GB, Glover GH, Hu BS, Enzmann DR. Pulsed magnetization transfer spin-echo MR imaging. J Magn Reson Imaging. 1993; 3(3):531–539. [PubMed: 8324313]
34. Jiang, X., van Gelderen, P., Li, X., Leibovitch, E., Sati, P., Silva, AC., Duyn, JH. Study of Bound Proton T2 and Magnetization Transfer using Pulsed MT. Toronto: ISMRM; 2015. p. 0998
35. van Gelderen, P., Jiang, X., Duyn, JH. Exploring a Flexible Pulse Design for Studying Magnetization Transfer. Toronto: ISMRM; 2015. p. 0996
36. Li AX, Suchy M, Jones CK, Hudson RH, Menon RS, Bartha R. Optimized MRI contrast for on-resonance proton exchange processes of PARACEST agents in biological systems. Magn Reson Med. 2009; 62(5):1282–1291. [PubMed: 19780147]
37. Vinogradov E, Zhang S, Lubag A, Balschi JA, Sherry AD, Lenkinski RE. On-resonance low B1 pulses for imaging of the effects of PARACEST agents. J Magn Reson. 2005; 176(1):54–63. [PubMed: 15979362]
38. Vinogradov E, He H, Lubag A, Balschi JA, Sherry AD, Lenkinski RE. MRI detection of paramagnetic chemical exchange effects in mice kidneys in vivo. Magn Reson Med. 2007; 58(4): 650–655. [PubMed: 17899603]
39. Yadav NN, Jones CK, Xu J, Bar-Shir A, Gilad AA, McMahon MT, Zijl PCMv. Detection of rapidly exchanging compounds using on-resonance frequency labeled exchange (FLEX) transfer. Magn Reson Med. 2012; 68:1048. [PubMed: 22837066]
40. Friedman JI, Xia D, Regatte RR, Jerschow A. Transfer Rate Edited experiment for the selective detection of Chemical Exchange via Saturation Transfer (TRE-CEST). J Magn Reson. 2015; 256:43–51. [PubMed: 25996515]
41. Davies NP, Summers IR, Vennart W. Optimum setting of binomial pulses for magnetization transfer contrast. J Magn Reson Imaging. 2000; 11(5):539–548. [PubMed: 10813864]
42. van Zijl PCM, Zhou J, Mori N, Payen J-F, Wilson D, Mori S. Mechanism of magnetization transfer during on-resonance water saturation. A new approach to detect mobile proteins, peptides, and lipids. Magn Reson Med. 2003; 49(3):440–449. [PubMed: 12594746]
43. Sled JG, Pike GB. Quantitative Interpretation of Magnetization Transfer in Spoiled Gradient Echo MRI Sequences. J Magn Reson. 2000; 145(1):24–36. [PubMed: 10873494]
44. Varma G, Duhamel G, de Bazelaire C, Alsop DC. Magnetization transfer from inhomogeneously broadened lines: A potential marker for myelin. Magn Reson Med. 2014 10.1002/mrm.25174.
45. Malyarenko DI, Zimmermann EM, Adler J, Swanson SD. Magnetization transfer in lamellar liquid crystals. Magn Reson Med. 2013
46. Qin Q, Grgac K, van Zijl PC. Determination of whole-brain oxygen extraction fractions by fast measurement of blood T(2) in the jugular vein. Magn Reson Med. 2011; 65(2):471–479. [PubMed: 21264936]
47. Xu, X., Yadav, NN., Zeng, H., Jones, C., Zhou, J., Zijl, Pv, Xu, J. MTC Free APT and RNOE-CEST Images of Human Brain at 7T. Milan: ISMRM; 2014. p. 0765
48. Gochberg DF, Gore JC. Quantitative imaging of magnetization transfer using an inversion recovery sequence. Magn Reson Med. 2003; 49(3):501–505. [PubMed: 12594753]
49. Zaiss M, Zu Z, Xu J, Schuenke P, Gochberg DF, Gore JC, Ladd ME, Bachert P. A combined analytical solution for chemical exchange saturation transfer and semi-solid magnetization transfer. NMR Biomed. 2015; 28(2):217–230. [PubMed: 25504828]
50. Cai K, Haris M, Singh A, Kogan F, Greenberg JH, Hariharan H, Detre JA, Reddy R. Magnetic resonance imaging of glutamate. Nat Med. 2012; 18(2):302–306. [PubMed: 22270722]
51. Walker-Samuel S, Ramasawmy R, Torrealdea F, Rega M, Rajkumar V, Johnson SP, Richardson S, Goncalves M, Parkes HG, Arstad E, Thomas DL, Pedley RB, Lythgoe MF, Golay X. In vivo imaging of glucose uptake and metabolism in tumors. Nat Med. 2013; 19(8):1067–1072. [PubMed: 23832090]

52. Haris M, Nanga RP, Singh A, Cai K, Kogan F, Hariharan H, Reddy R. Exchange rates of creatine kinase metabolites: feasibility of imaging creatine by chemical exchange saturation transfer MRI. NMR Biomed. 2012; 25(11):1305–1309. [PubMed: 22431193]

53. Yadav NN, Xu JD, Bar-Shir A, Qin Q, Chan KWY, Grgac K, Li WB, McMahon MT, van Zijl PCM. Natural D-Glucose as a Biodegradable MRI Relaxation Agent. Magn Reson Med. 2014; 72(3):823–828. [PubMed: 24975029]

54. Gore JC, Brown MS, Mizumoto CT, Armitage IM. Influence of Glycogen on Water Proton Relaxation-Times. Magn Reson Med. 1986; 3(3):463–466. [PubMed: 3724426]

55. Kucharczyk W, Macdonald PM, Stanisz GJ, Henkelman RM. Relaxivity and magnetization transfer of white matter lipids at MR imaging: importance of cerebrosides and pH. Radiology. 1994; 192(2):521–529. [PubMed: 8029426]

56. Stikov N, Perry LM, Mezer A, Rykhlevskaia E, Wandell BA, Pauly JM, Dougherty RF. Bound pool fractions complement diffusion measures to describe white matter micro and macrostructure. NeuroImage. 2011; 54(2):1112–1121. [PubMed: 20828622]

57. Xu X, Yadav NN, Zeng H, Jones C, Zhou J, Zijl Pv, Xu J. Magnetization transfer contrast–suppressed imaging of amide proton transfer and relayed nuclear overhauser enhancement chemical exchange saturation transfer effects in the human brain at 7T. Magn Reson Med. 2016; 75(1):88–96. [PubMed: 26445350]

58. Snoussi K, Gillen JS, Horska A, Puts NA, Pradhan S, Edden RA, Barker PB. Comparison of brain gray and white matter macromolecule resonances at 3 and 7 Tesla. Magn Reson Med. 2015; 74(3): 607–613. [PubMed: 25252131]

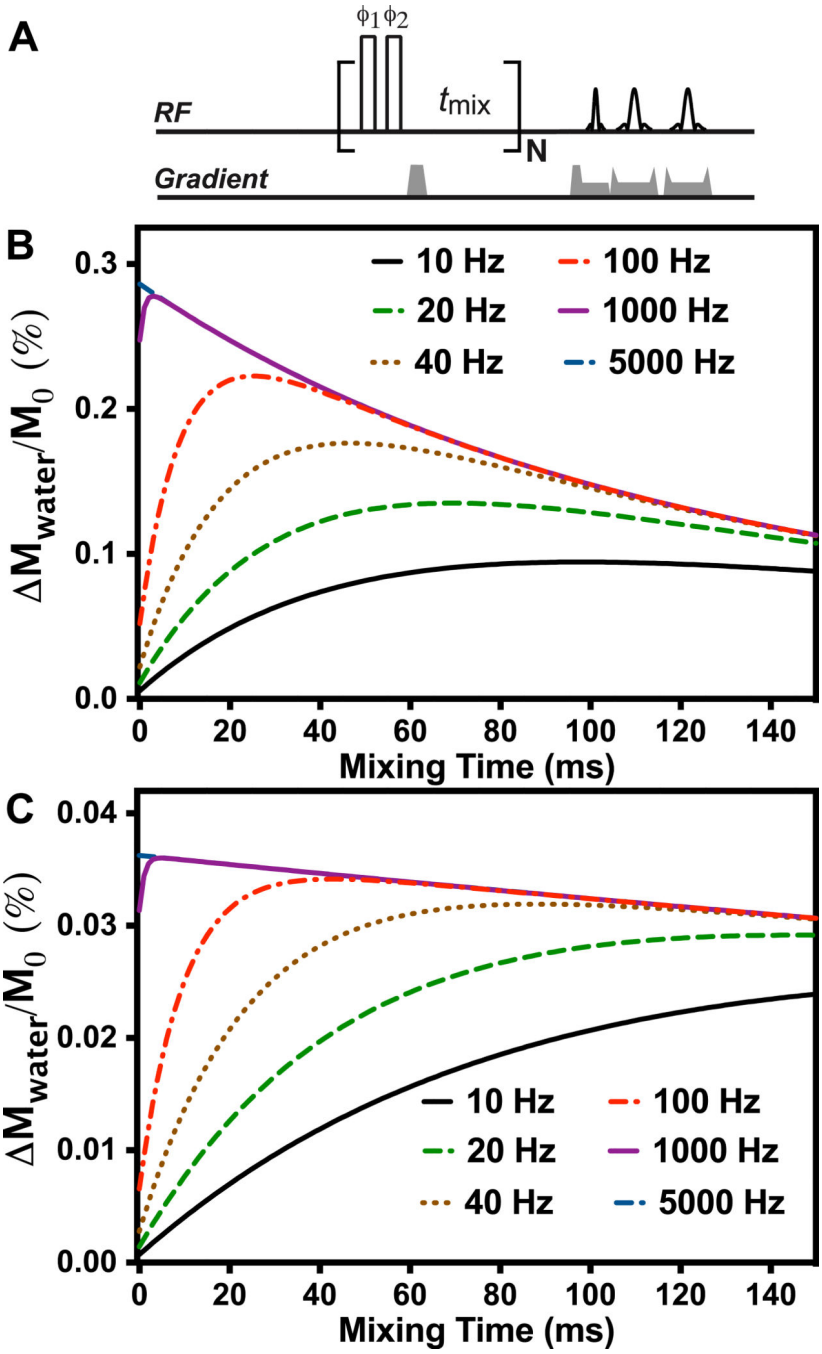

Figure 1.

(A) On-resonance VDMP sequence with cyling of the pulses over four label transfer modules (LTMs) by ϕ1 = x y −x −y; ϕ2 = −x −y x y. Open rectangles represent hard pulses. Simulation of the VDMP buildup curves for different exchange rates with 32 (B) and 4 binomial pulses (C). In the simulations, 2-ms pulses with B_1 field of 93.6 μT was applied; An exchanging proton concentration of 20 mM and an offset of 2 ppm was assumed. The relaxation times of water and the exchanging protons were set to 2 s and 1s, respectively.

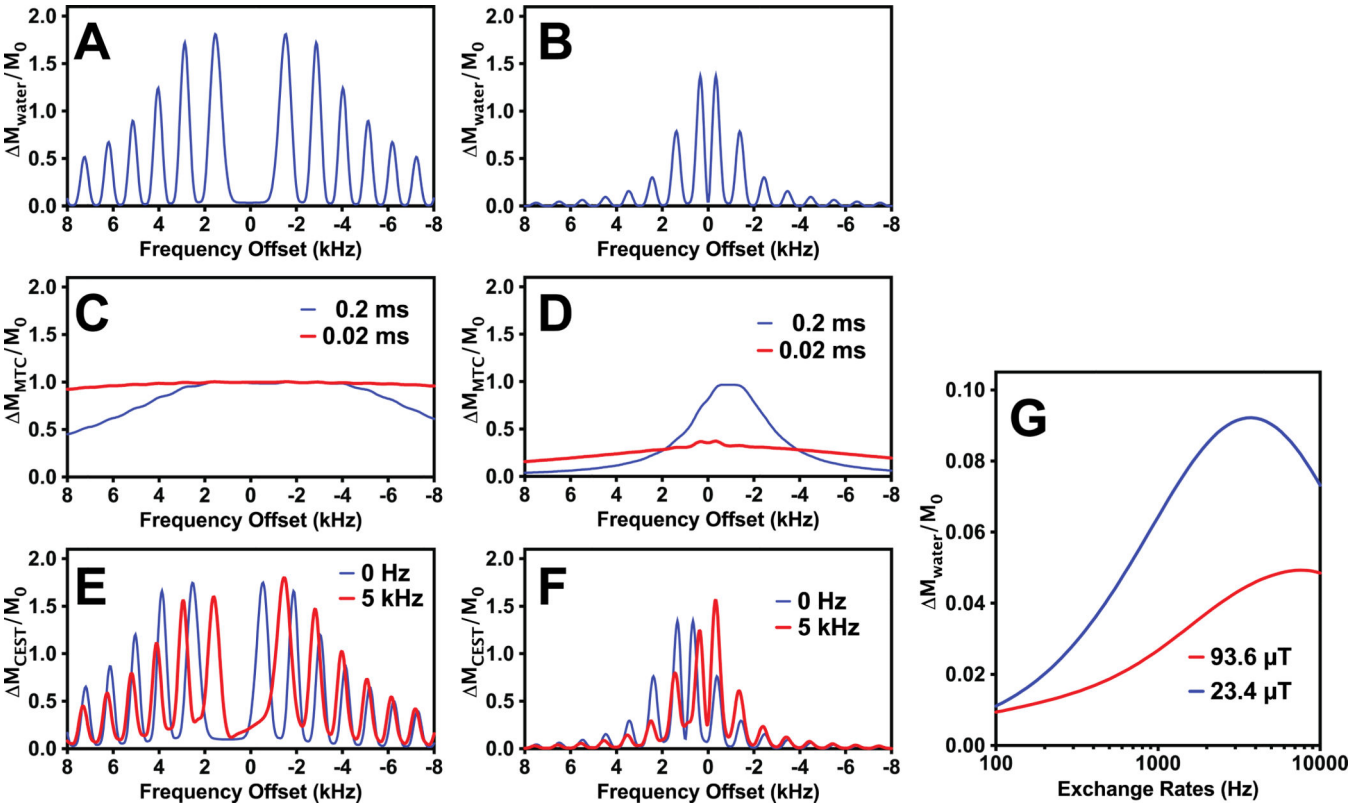

Figure 2.

(A–F) Pulse excitation profiles of the binomial pulse ($p\bar{p}$) for the water pool (A and B), MTC pool (C and D) and exchanging proton (CEST) pool (E and F). Two B_1 values, 93.6 μT (A, C and E) and 23.4μT (B, D and F), were simulated with 2 ms pulse width. In the simulations, T_2 = 30 ms was used for the water pool. For the MTC pool, two typical T_2 values (0.2 and 0.02 ms) with an exchange rate of 30 Hz were used, while T_2 = 10 ms and exchange rates of 0 Hz and 5 kHz were applied for the exchanging solute protons. The center of the MTC pool was set to −2 ppm. The chemical shift of the exchanging solute protons was 2 ppm. (G) The water signal reduction due to CEST effect as a function of exchange rate for two typical saturation powers (93.6 and 23.4 μT,) of the binomial pulse.

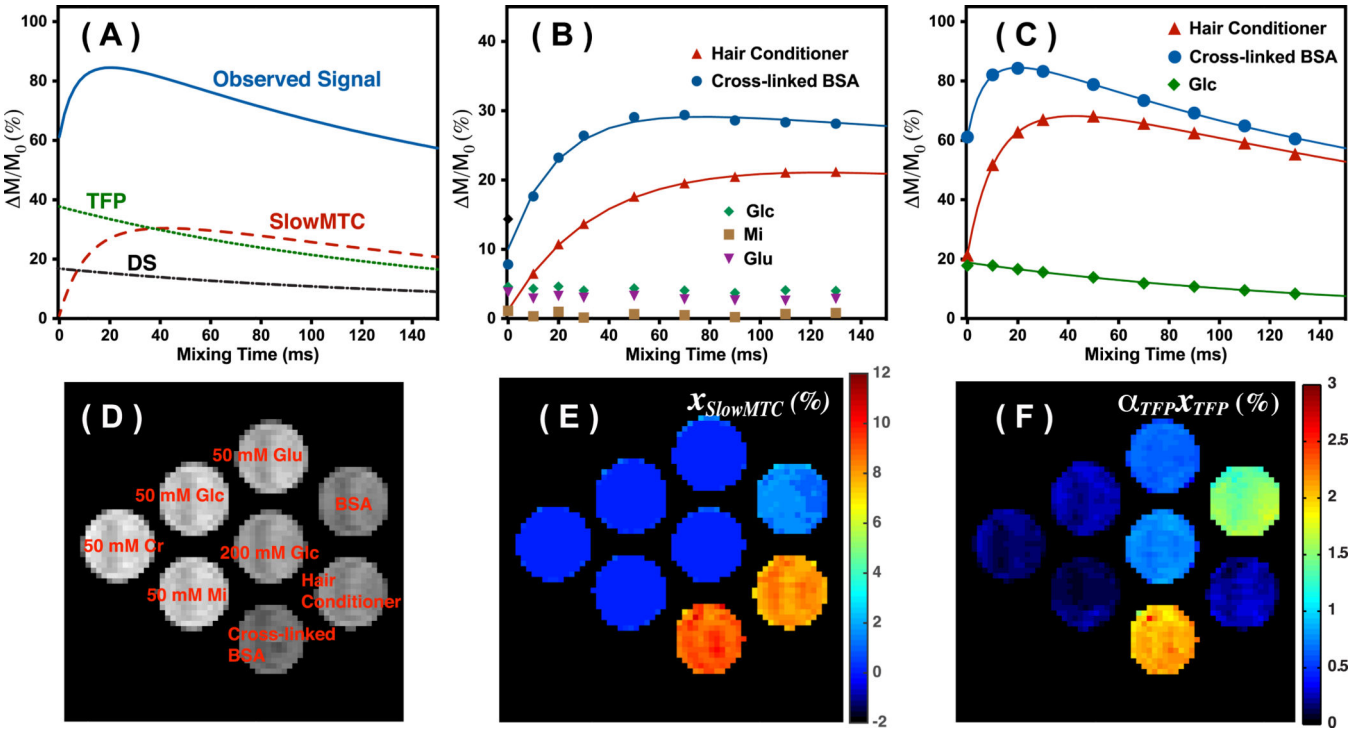

Figure 3.

(A) Simulation of the three contributions in the observed VDMP buildup curves, and their typical patterns for on-resonance VDMP excitation: DS, slowMTC and TFP. (B) VDMP buildup curves for hair conditioner, cross-linked BSA, MI (50 mM), Glu (50 mM) and Glc (200 mM) recorded using four binomial pulses (2 ms, 93.6 μT). The solid lines are the fitted curves using the 2-pool Bloch simulations. (C) The VDMP buildup curves obtained using 32 binomial pulses (2 ms, 93.6 μT) for hair conditioner, cross-linked BSA and Glc (200 mM) are plotted together with the fitted curves from the 3-pool model. (D) M0 image together with the labels for the phantoms. (E) The slowMTC population fraction map calculated for the 32-pulse situation using Eq.2 with a two-pool model. (F) The $\bar{\alpha}_{TFP}x_{TFP}$ population fraction map as percent of the water signal calculated assuming a three-pool model.

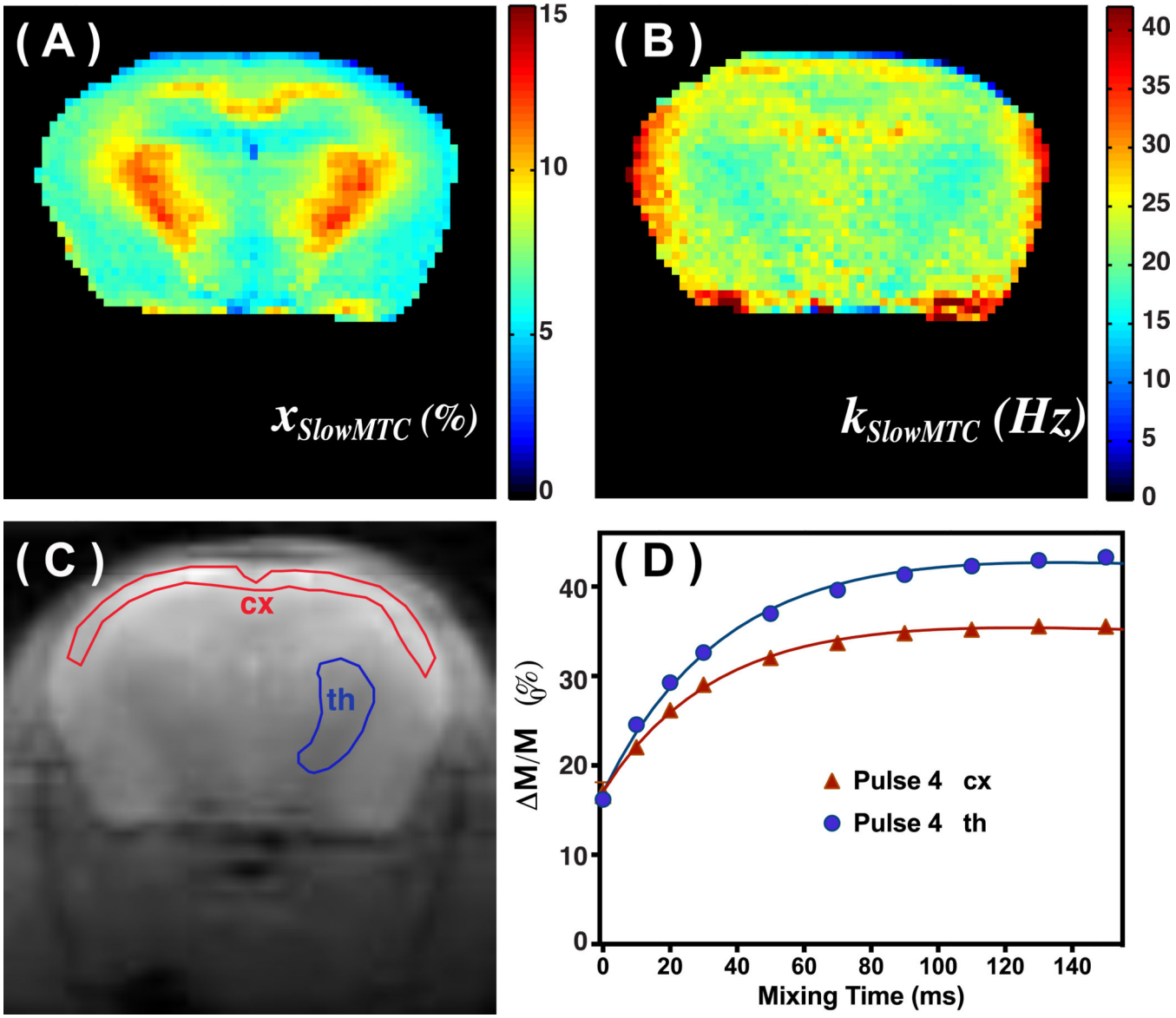

Figure 4.

$x_{slowMTC}$ (A) and exchange rate $k_{slowMTC}$ maps (B) of mouse brain calculated from the VDMP buildup curves resulting from four binomial pulses (2ms, 93.6 μT) and fitted using a two-pool model. (C) The M0 images recorded on the same slice of the mouse brain. The ROIs for obtaining the VDMP buildup curves are labeled. (D) The corresponding VDMP buildup curves of the cortex (cx) and thalamus (th) together with fitted curves.

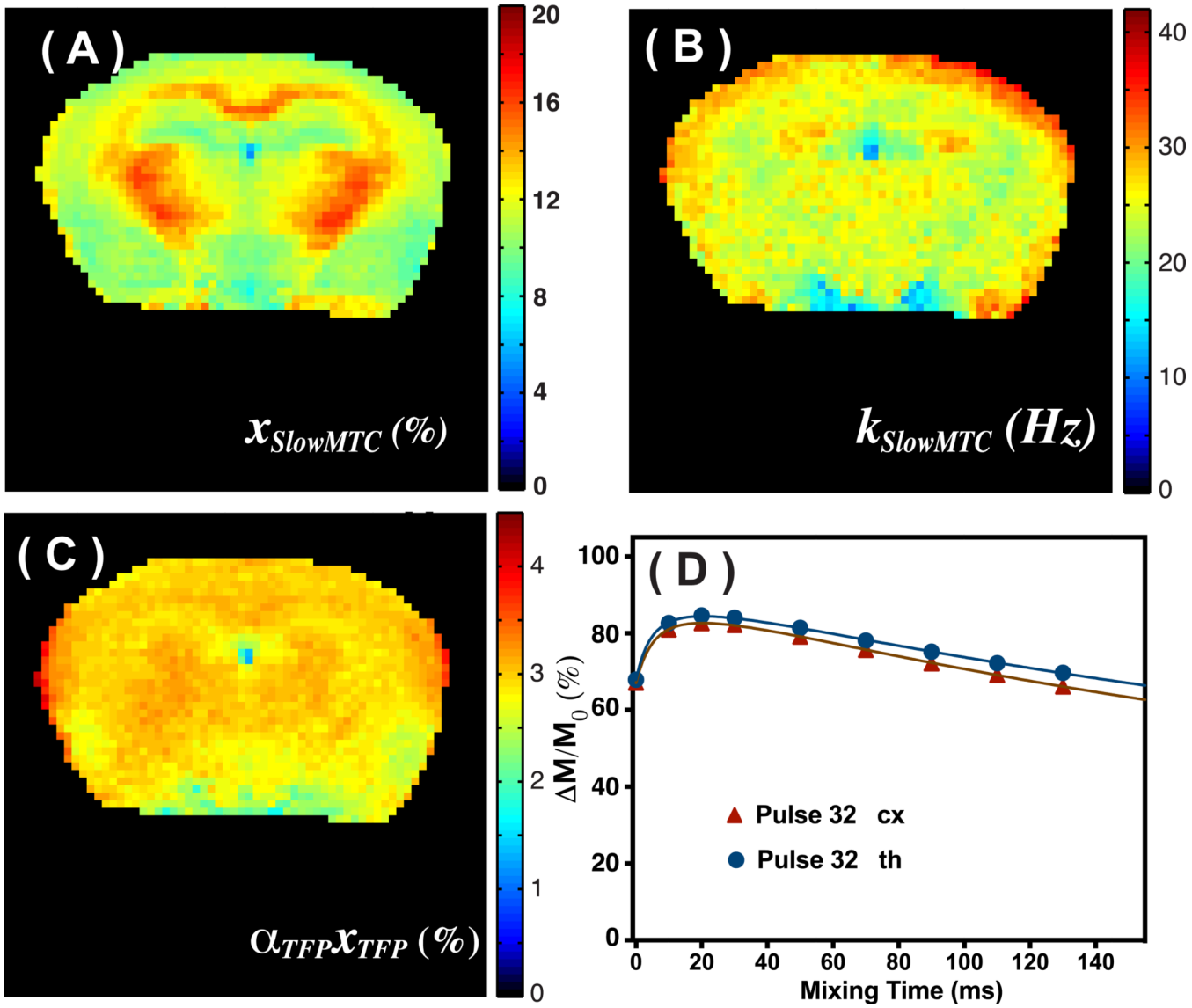

Figure 5.

$x_{slowMTC}$ (A), exchange rate $k_{slowMTC}$ (B) and $\bar{\alpha}_{TFP}x_{TFP}$ maps (C) of mouse brain calculated from the VDMP buildup curves resulting from 32 binomial pulses (2 ms, 93.6 μT) and fitted using a three-pool model. (D) The corresponding VDMP buildup curves of cx, and th together with fitted curves.

Table 1

The T_1 and T_2 relaxation times, $x_{slowMTC}$, exchange rates $k_{slowMTC}$ and $\bar{\alpha}_{TFP}x_{TFP}$ measured on the phantoms. With low concentration of $x_{slowMTC}$, the exchange rates $k_{slowMTC}$ are difficult to be measured reliably, and not listed.

Samples	Cross-linked BSA	Hair Conditioner	BSA	Glu 50 mM	Glc 200mM	Glc 50 mM	MI	Cr
T_1 (s)	1.7	2.0	1.9	2.6	2.5	2.9	2.7	2.9
T_2 (ms)	52.9	117.4	59.5	187.3	89.0	356.5	316.2	484.5
$x_{slowMTC}$ (%) *a*	9.3±0.4	7.7±0.5	1.5±0.05	0.1±0.1	0.2±0.2	0	0	0
b	8.0±0.8	8.7±1	2.7±0.5	0.2±0.1	0.2±0.1	0.3±0.05	0.3±0.05	0.3±0.05
$k_{slowMTC}$ (Hz)[a]	57.3±8	22.9±2	\	\	\	\	\	\
b	46.6±6	21.6±0.3	\	\	\	\	\	\
$\bar{\alpha}_{TFP}x_{TFP}$ (%)[b]	2.4±0.4	0.25±0.02	1.9±0.4	0.61±0.05	0.74±0.03	0.19±0.04	0.11±0.01	0.14±0.01

[a] Values obtained by fitting VDMP buildup curves with four pulses using two parameters.

[b] Values obtained by fitting VDMP buildup curves with 32 pulses using four parameters.

Table 2

Fitted MTC fractions $x_{slowMTC}$, exchange rates $k_{slowMTC}$, and $\bar{\alpha}_{TFP}x_{TFP}$ measured *in vivo*.

	Cortex	thalamus
$x_{slowMTC}$ (%)[a]	6.4 ± 0.5	9.8 ± 0.7
b	11.0 ± 0.7	14.7 ± 0.9
$k_{slowMTC}$ (Hz)[a]	23.4± 1.5	19.7± 1.5
b	24.5 ± 1.8	24.5 ± 1.8
$\bar{\alpha}_{TFP}x_{TFP}$ (%)[b]	3.0 ± 0.15	3.0 ± 0.15

[a]Values obtained by fitting VDMP buildup curves with four pulses using two parameters.

[b]Values obtained by fitting VDMP buildup curves with 32 pulses using four parameters.

[*]errors are standard deviation over the ROI